# An Isolated Triple-Active-Bridge Converter With Highly Dynamic and Adaptive Power Decoupling Control

Hui Cao, *Student Member, IEEE*, Guangqi Zhu, *Member, IEEE*, Xinze Li, *Member, IEEE*,
Peyman Darvish, *Graduate Student Member, IEEE*, and Yue Zhao, *Senior Member, IEEE*

***Abstract*—In this article, highly dynamic and adaptive power decoupling control methods are proposed for isolated triple-active-bridge (TAB) converters to address various cross-coupling related challenges. First, novel decoupling methods are derived analytically from system modeling of TAB and multiple-input-multiple-output system decomposition strategies to mitigate the power cross-coupling issue among dc ports. Unlike the conventional approaches, the proposed methods adapt the decoupling network to varying operating conditions to ensure improved decoupling performance. Second, a feedforward method is proposed to calculate the target operating phase shifts online effectively, which is integrated with the proposed decoupling network to enhance dynamic performance while maintaining good controllability across the entire power range. Furthermore, the robustness of TAB converter is improved through the proposed decoupling control methods. Finally, comparative simulations and experimental results validate the superiority of the proposed decoupling strategies over conventional approaches.**

***Index Terms*—Control, dc–dc converter, decoupling method, feedforward (FF), triple-active-bridge (TAB).**

## I. INTRODUCTION

THE isolated dual-active-bridge (DAB) converters have been adopted in many applications, e.g., the renewable energy conversion systems, solid-state transformers (SSTs), electric vehicles (EVs), and uninterrupted power supplies (UPS), due to their distinctive advantages, such as the intrinsic galvanic isolation, bidirectional power transmission, soft switching capability, and wide operating range [1]. The three-port isolated triple-active-bridge (TAB) converter, as shown in Fig. 1, is an extension of DAB. The TAB, on one hand, retains most of the benefits of DAB, on the other hand, is feasible and effective to interface multiple sources with less components. The use of a three-winding transformer in a TAB can lead to substantial weight reduction [2], [3]. The multiport nature of TAB makes it suitable for multiport applications, enabling flexible power flow management among diverse sources, storage and loads.

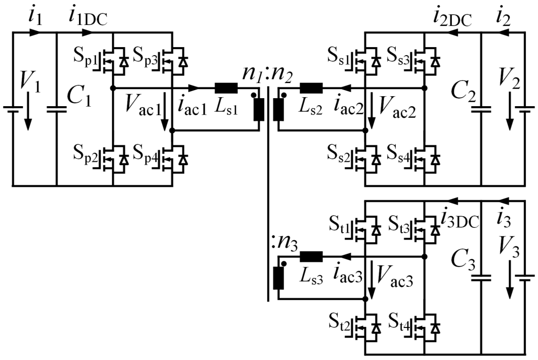

Fig. 1. Isolated three-port TAB DC–DC converter.

To interface the diverse energy sources, storage elements, and loads, TABs are becoming increasingly popular in various multiport converter applications: EVs, fuel cell vehicles (FCVs), UPS, dc microgrids, etc. [2]. In EVs and FCVs, energy storage devices work as an essential element for capturing regenerative brake and energy release during startup and acceleration. In photovoltaic system, battery energy storage system is also integrated to balance the fluctuation of solar power generation and smooth the output power profile. DC renewable energy sources, storage devices and loads are conventionally interfaced with separate single-stage or multistage power conversion converters in dc microgrids [3]. In those multiport applications, the essential TAB converter is able to interconnect multiple sources, storage, loads, and multiple voltage grids using a minimum number of power conversion stages and components while maintaining full controllability of the bidirectional power flow. Thus, the cost, size, and volume of the whole power conversion system can be highly reduced due to less devices and compact high frequency transformer. The TAB converter based single power conversion stage system results in higher power density and efficiency [2].

Although the nature of TAB converter has benefits for multiple ports system applications, the separate multiple dc ports interfaced by TAB converter will lead to the cross-coupling issue of power flow among the multiple dc ports. Changes in the phase

---

Received 19 March 2025; revised 26 June 2025 and 7 September 2025; accepted 4 October 2025. Date of publication 10 October 2025; date of current version 19 January 2026. This work was supported by the U.S. National Science Foundation (NSF) Center on Grid Connected Advanced Power Electronic Systems (GRAPES). Recommended for publication by Associate Editor Y. Siwakoti. *(Corresponding author: Yue Zhao.)*

Hui Cao, Xinze Li, Peyman Darvish, and Yue Zhao are with the Department of Electrical Engineering and Computer Science, University of Arkansas, Fayetteville, AR 72701 USA (e-mail: hcao@uark.edu; xinzel@uark.edu; darvish@uark.edu; yuezhao@uark.edu).

Guangqi Zhu is with Eaton Research Labs, Eaton Corporation, Menomonee Falls, WI 53051 USA (e-mail: guangqizhu@hotmail.com).

Color versions of one or more figures in this article are available at https://doi.org/10.1109/TPEL.2025.3620241.

Digital Object Identifier 10.1109/TPEL.2025.3620241

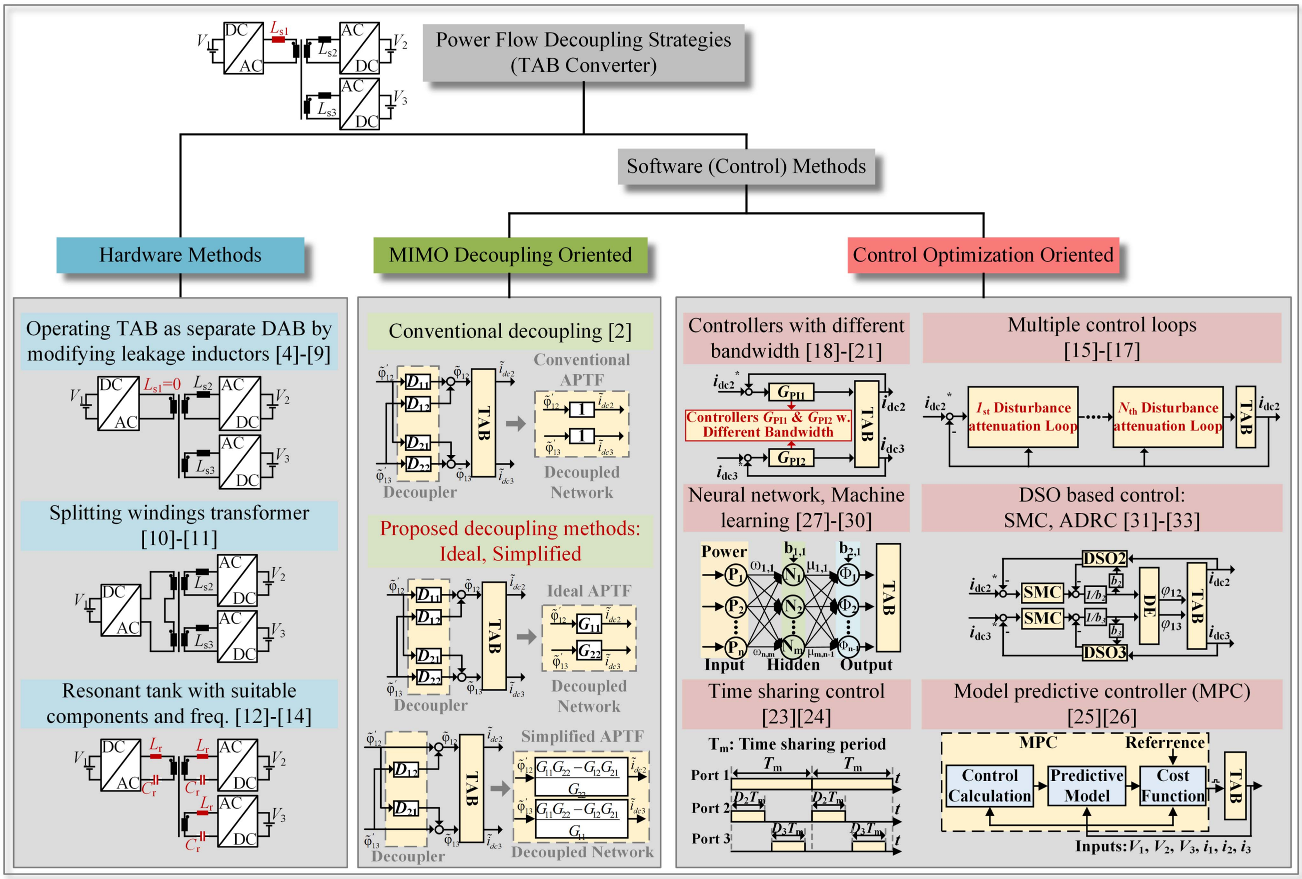

Fig. 2. Different decoupling methods in literature.

TABLE I
COMPARISON OF DIFFERENT DECOUPLING METHOD

| Comparisons | Decoupling Methods | | | | | | | | | | | |
|---|---|---|---|---|---|---|---|---|---|---|---|---|
| | Hardware | | | Software Control Oriented | | | | | | | | |
| | | | | Control Optimization Oriented | | | | | | | MIMO Decoupling | |
| | [4]-[9] | [10]-[11] | [12]-[14] | [15]-[17] | [18]-[21] | [23]-[24] | [25]-[26] | [27]-[30] | [31]-[33] | [34] | [2] | Proposed |
| Physical Modification | Yes | Yes | Yes | No | No | No | No | No | No | No | No | No |
| Bidirectional | No | No | No | Yes | Yes | Yes | Yes | Yes | Yes | No | Yes | Yes |
| FF | No | No | No | No | No | No | No | No | No | Yes | Yes | Yes |
| Universality | No | No | No | Yes | Yes | Yes | Yes | Yes | Yes | No | Yes | Yes |
| Adaptive | No | No | No | No | No | No | No | No | No | No | No | Yes |
| Flexibility | N/A | N/A | N/A | moderate | moderate | moderate | Good | Good | Good | moderate | Good | Good |
| Complexity | Medium | Complex | Complex | Simple | Simple | Simple | Medium | Complex | Medium | Complex | Medium | Medium |

shift angle $\varphi_{12}$ to control the secondary dc port's power flow $P_2$ will also affect another two dc ports' power flow $P_1$ and $P_3$, vice versa. In this work, the interaction of dc power flows manifests itself as dc ports' current disturbance, because current control is adopted with pump-back test. Its cross-coupling issue between different ports can lead to excessive voltage/current overshoots, poor dynamic performance and reduced system controllability. Because the dc output ports of TAB converter are cross-coupled as a typical multi-input-multioutput (MIMO) system, according to the control-to-output transfer function of TAB converter as shown in (12) and (13). Therefore, a decoupling network $D_{ij}$ is critical for TAB to decompose a MIMO system into several independent single-input-single-output (SISO) systems [2].

The decoupling of the TAB converter can be achieved through the modifications of hardware and software (or control based) methods as summarized in Fig. 2 and Table I. Various hardware modification methods have been proposed to achieve power decoupling. For instance, a TAB converter can be operated as separate DAB converters using modified leakage inductors [4], [5]; or by removing the external inductor from one port of the TAB and properly designing the transformer and the remaining two leakage inductors [6], [7], [8]. However, the control design in these cases requires special attention due to the asymmetric characteristics and nonlinearity of the TAB converter. A similar method is presented in [9], where one port is designed with a small series inductance, and a dynamically reconfigurable bridge is proposed to maintain decoupled power flow when the main low-inductance port fails. Another approach involves splitting the three-winding transformer in a TAB into two two-winding transformers [10], [11]. In addition, the resonant tank can be decoupled by selecting appropriate resonant elements and tuning the resonant frequency [12], [13], [14].

These hardware-based decoupling strategies require physical modifications to the TAB converter, which are typically tailored to specific applications and may not be adaptable to others. Furthermore, these approaches introduce additional challenges, such as the potential loss of bidirectional power transfer capability, increased system cost, and higher losses.

The control-based software methods can address cross-coupling issues without hardware modifications. Decoupling can be achieved using controller architecture with multiple control loops [15], [16], [17] or involving multiple controllers with different bandwidth [18], [19], [20], [21], which can lead to acceptable dynamic performance with fine-tuned controller design [22]. Time sharing control can reduce the interaction between different ports by operating the TAB converter as a DAB converter at each time instant and limiting its functionality to only specific use cases [23], [24]. Some nonlinear control methods are proposed for the multiactive-bridge converters, e.g., model predictive controller in [25] and [26] provides a moderate dynamic response with higher steady-state error. Neural network [27] and machine learning [28] based decoupling controls have also been explored. A look-up table combined with an artificial neural network is used to simplify the control design; however, the overall implementation remains complex [29], [30]. These methods are data-intensive and case-specific, making them more suitable for converters with a higher number of ports. The disturbance observer based control techniques, such as sliding mode control [31], active disturbance rejection control [32], and super-twisting algorithm [33], mitigate the cross-coupling effect by treating it as a form of disturbance, which is essentially control optimization instead of decoupling. Power decoupling modulation is proposed in [34]. Although this modulation technique can mitigate the coupling issue, it limits the TAB to operate as two independent DAB converters. Moreover, the modulation is complex to implement and is highly sensitive to model accuracy.

In contrast to the previously mentioned control-optimization-based methods for mitigating cross-coupling issues in TAB converters, the commonly used decoupling method in [2], when the TAB was first proposed, is to decouple the two-input-two output (TITO) system into a SISO system for TAB converter. This conventional method is adopted in this work as a baseline for comparison. However, it loses essential system characteristics by integrating the decoupling network—i.e., the inverse of the system matrix—as a fixed unit-gain schedule. As a result, the dynamic response of the TAB converter becomes insufficient for highly dynamic applications, especially during transitions between forward and reverse power flow operations.

To address the limitations of existing hardware and software decoupling methods, this article proposed adaptive and highly dynamic decoupling control strategies. In the software control method based on "MIMO decoupling oriented" classification, as shown in Fig. 2, the proposed methods decouple the TITO system into an independent SISO system while preserving the essential characteristics of the TAB converter to ensure adaptive decoupling and highly dynamic performance. The proposed adaptive decoupling control methods effectively mitigate power flow interactions among the dc ports without compromising dynamic performance. Instead, they significantly improve the system's dynamic respond speed and reduce overshoot, while maintaining good controllability.

Another major challenge in decoupling network design is the inherent nonlinearity of TAB converters. To address this, a feedforward (FF) design is proposed in this work to compute the target phase shift angles required for operation, thereby overcoming the nonlinearity issue. Although FF computation requires significant processing power, this was a limiting factor when the TAB was first proposed in 2002. However, with the rapid advancement in computational capabilities, modern cost-effective chips are powerful enough to support real-time calculation of the FF loop. The Newton-Raphson iteration method is adopted to solve the FF equations for the target phase shift angles.

The technical challenges associated with the dc ports' interaction in a TAB converter can be mitigated with oversized system design, such as capacitor, transformer, and inductor, leading to higher system cost, worse dynamic performance, and poor power density. In contrast, these issues can be fully or substantially addressed through cost-effective decoupling control design for the TAB converter. The main contributions of this article are as follows.

1) A FF algorithm is designed to calculate the target operating phase shift angles of TAB converter and feed the target operating points to the decoupling network, which helps to maintain good controllability over the full power range.
2) Highly dynamic and adaptive decoupling control methods are proposed to address the cross-coupling of the power flows between different ports of the TAB. The dc ports' oscillations are reduced with proposed methods without sacrificing the dynamic response time. What is more, the proposed methods are adaptive to the system changes to improve dynamic performance, such as varying operation points and dc voltages. In addition, the controllability is improved for TAB across the full power range.
3) Comprehensive studies and comparisons of adaptive decoupling control strategies are conducted. The effectiveness and adaptiveness of proposed decoupling control methods and FF algorithm is validated in practical applications, supported by detailed theoretical analysis and scaled-down 10 kW experimental studies.

The rest of this article is organized as follows. First, a detailed FF is introduced for the TAB converter in Section II. Then, highly dynamic decoupling methods are proposed with detailed design and theoretical analysis in Section III. Finally, the effectiveness of the proposed decoupling control methods is validated with dedicated experimental studies in Section IV. Section V concludes this article.

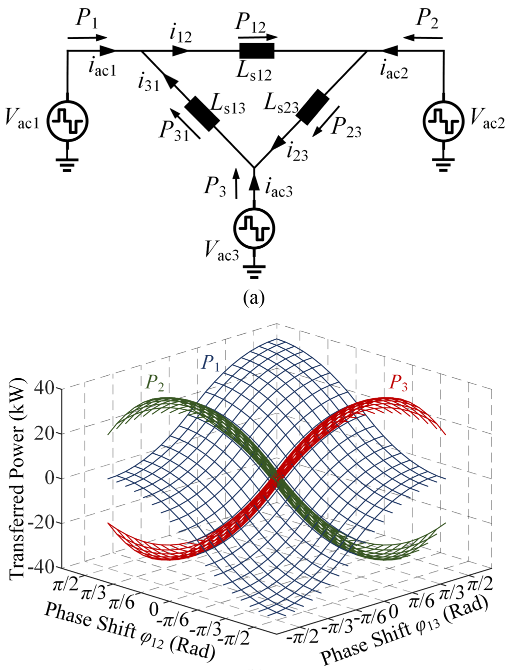

(a)

(b)

Fig. 3. (a) Delta equivalent circuit of TAB converter. (b) TAB's transferred power versus phase shift angles.

## II. FF Design for TAB Converter

Since the decoupling network design is based on the real-time target operating points of the TAB converter, the power model and FF design are presented first. The operating principles of the SPS modulation for the TAB converter have been presented in [2]. In this work, definitions for all variables in a TAB shown in Fig. 1 are referred to the primary side. The dc voltages across the primary, secondary, and tertiary dc ports are denoted as $V_1$, $V_2$, and $V_3$, respectively. Then, the voltages across the three-winding transformer can be determined as $|V_{\rm ac1}| = V_1$, $|V_{\rm ac2}| = V_2$, $|V_{\rm ac3}| = V_3$. The powers of the three dc ports are defined as $P_1$, $P_2$, and $P_3$. The leakage inductances of TAB are represented by $L_{\rm s1}$, $L_{\rm s2}$, $L_{\rm s3}$ in $Y$ model, while the number of turns in the transformer windings are $n_1$, $n_2$, and $n_3$, while the corresponding turn ratios are represented as $N_{\rm tr12}$, $N_{\rm tr23}$, $N_{\rm tr13}$, respectively. The $\varphi_{12}$, $\varphi_{13}$, and $\varphi_{23}$ are the phase shift angles of gate signal between $V_{\rm ac1}$ and $V_{\rm ac2}$, $V_{\rm ac1}$ and $V_{\rm ac3}$, $V_{\rm ac2}$, and $V_{\rm ac3}$, respectively. The dc port's currents are defined as $i_1$, $i_2$, $i_3$, the dc link currents are represented by $i_{\rm dc1}$, $i_{\rm dc2}$, $i_{\rm dc3}$, respectively. The power flows between the three ports are controlled bidirectionally by manipulating the phase shift angles in the range of $[-\pi/2,\ \pi/2]$. The conversion of the leakage inductance between $Y$ model and $\Delta$ model can be simplified as follows:

$$\begin{aligned} L_{s12} &= L_{s1} + L_{s2} + L_{s1}L_{s2}/L_{s3} \\ L_{s23} &= L_{s2} + L_{s3} + L_{s2}L_{s3}/L_{s1} \\ L_{s31} &= L_{s1} + L_{s3} + L_{s1}L_{s3}/L_{s2}. \end{aligned} \tag{1}$$

Since the DAB converter is a typical nonlinear system, to maintain a good controllability at low power range, normally, the maximum phase shift of DAB converter at rated power is restricted to [π/4, π/3] [35]. The TAB converter, as an extension of DAB, cross-coupling issues even worsen its controllability. On the other hand, the decoupling network design is based on the target operating point of TAB converter to obtain its system matrix information. Therefore, a FF block is designed to calculate the phase shifts of the target operating point for TAB converter and feed the target operating points to the decoupling network, which helps to address the issue of limited control range and maintains good controllability over full power range.

TABLE II
Specifications of Experimental TAB Converter

| | |
|---|---|
| DC port's voltages | $V_1 = V_2 = V_3 = 300$ V |
| DC port's currents | $i_1$, $i_2$, $i_3$ |
| DC link's currents | $i_{\rm dc1}$, $i_{\rm dc2}$, $i_{\rm dc3}$ |
| DC port's power flows | $P_1$, $P_2$, $P_3$ |
| Transformer's AC voltages | $V_{\rm ac1}$, $V_{\rm ac2}$, $V_{\rm ac3}$ |
| Leakage inductances $L_{\rm si}$ | $L_{\rm s1} = L_{\rm s2} = L_{\rm s3} = 20\ \mu$H |
| Transformer turns ratios $N_{\rm tr\mathit{ij}}$ | $N_{\rm tr12} = N_{\rm tr23} = N_{\rm tr13} = 1$ |
| Phase shift angles $\varphi_{ij}$ | $\varphi_{12}$, $\varphi_{13}$, $\varphi_{23}$ |
| Switching frequency | $f_{\rm sw} = 10$ kHz |

For given phase shift angles $\varphi_{ij}$, the power flow $P_{ij}$ transferred from port *i* to port *j* between TAB converter can be derived using the equations well-known from the conventional DAB converter [1]

$$P_{ij} = \frac{V_i V_j N_{trij}}{2\pi f_{sw} L_{sij}} \cdot \left(\varphi_{ij} - \varphi_{ij}^2/\pi\right) \tag{2}$$

where $i, j \in \{1, 2, 3\} \wedge i \neq j)$, $V_i$ and $V_j$ are the dc port voltages. From the equivalent circuit of TAB converter as shown in Fig. 3(a), the following set of equations can be derived for TAB converter as shown in the following equation:

$$\begin{aligned} P_1 &= P_{12} - P_{31} \\ P_2 &= -P_{12} + P_{23} \\ P_3 &= P_{31} - P_{23}. \end{aligned} \tag{3}$$

Considering $P_{12} + P_{23} + P_{31} = 0$, the detailed system model of TAB can be derived in the following equation: (4) shown at the bottom of next page.

Based on parameters of the prototype used in the experiment in Table II, the relationship between dc port's power flows and phase shifts is shown in Fig. 3. The phase shifts $\varphi_{\rm 12FF}$ and $\varphi_{\rm 13FF}$ of target operating point of TAB can be calculated from the following equation using Newton's iterative method to solve the cubic equation

$$\begin{aligned} \varphi_{\rm 12FF} &= f_{12}\left(P_2, P_3, V_1, V_2, V_3\right) \\ \varphi_{\rm 13FF} &= f_{13}\left(P_2, P_3, V_1, V_2, V_3\right). \end{aligned} \tag{5}$$

In numerical analysis, the Newton-Raphson iteration method can successively approximate the root of a real-valued function $f(\varphi_N) = 0$, with its derivative $f^{'}(\varphi_N) = J(\varphi_N)$, represented as a

Jacobian matrix in this work, as shown in the following equation:

$$\varphi_{N+1} = \varphi_N - \frac{f\left(\varphi_N\right)}{J\left(\varphi_N\right)} \tag{6}$$

where the approximate root matrix $\varphi_N$ consists of two independent control variables $\varphi_{12}$ and $\varphi_{13}$, as well as the calculated phase shift angle $\varphi_{23}$. The basic real-valued function is the difference between every iterated port power and target ports power on the secondary and tertiary ports, respectively

$$\varphi_N = \begin{bmatrix} \varphi_{12} \\ \varphi_{13} \\ \varphi_{23} \end{bmatrix} \quad \text{and} \quad f\left(\varphi_N\right) = \begin{bmatrix} P_2(\varphi_N) - P_2^* \\ P_3(\varphi_N) - P_3^* \end{bmatrix}. \tag{7}$$

The derivative of $f(\varphi_N)$ is described in (8) with a Jacobian matrix $J(\varphi_N)$

$$J\left(\varphi_N\right) = \begin{bmatrix} \frac{dP_2}{d\varphi_{12}} & \frac{dP_2}{d\varphi_{13}} \\ \frac{dP_3}{d\varphi_{12}} & \frac{dP_3}{d\varphi_{13}} \end{bmatrix}. \tag{8}$$

The detailed element $J_{i,j}$ of the Jacobian matrix are given in (9)–(11), which are essential for the FF loop design.

For the power flow between port 1 and port 2

$$P_{12} = \frac{V_1 V_2 N_{tr12}}{2\pi f_{sw} L_{s12}} \cdot \left(\varphi_{12} - \varphi_{12}^2/\pi\right)$$

$$\frac{dP_{12}}{d\varphi_{12}} = \frac{V_1 V_2 N_{tr12}}{2\pi f_{sw} L_{s12}} \cdot \left(1 - 2\varphi_{12}/\pi\right) \text{and} \frac{dP_{12}}{d\varphi_{13}} = 0. \tag{9}$$

For the power flow between port 1 and port 3

$$P_{13} = \frac{V_1 V_3 N_{tr13}}{2\pi f_{sw} L_{s13}} \cdot \left(\varphi_{13} - \varphi_{13}^2/\pi\right)$$

$$\frac{dP_{13}}{d\varphi_{13}} = 0 \text{and} \frac{dP_{13}}{d\varphi_{13}} = \frac{V_1 V_3 N_{tr13}}{2\pi f_{sw} L_{s13}} \cdot \left(1 - 2\varphi_{13}/\pi\right). \tag{10}$$

For the power flow between port 2 and port 3

$$P_{23} = \frac{V_2 V_3 N_{tr23}}{2\pi f_{sw} L_{s23}} \cdot \left[\left(\varphi_{13} - \varphi_{12}\right) - \left(\varphi_{13} - \varphi_{12}\right)^2 \Big/ \pi\right]$$

$$\frac{dP_{23}}{d\varphi_{12}} = \frac{V_2 V_3 N_{tr23}}{2\pi f_{sw} L_{s23}} \cdot \left[-1 + 2\left(\varphi_{13} - \varphi_{12}\right)/\pi\right]$$

$$\frac{dP_{23}}{d\varphi_{13}} = \frac{V_2 V_3 N_{tr23}}{2\pi f_{sw} L_{s23}} \cdot \left[1 - 2\left(\varphi_{13} - \varphi_{12}\right)/\pi\right]. \tag{11}$$

Given that the operating phase shift angles in the range of [0, π/2] for forward power transmission, similarly, the operating phase shift angles in the range of [−π/2, 0] for backward power transmission, thus, an initial guess of the control variables $\varphi_N$ is set to be $\varphi_N = [0, 0]$ to start the iteration process of the proposed FF loop as shown in Fig. 4.

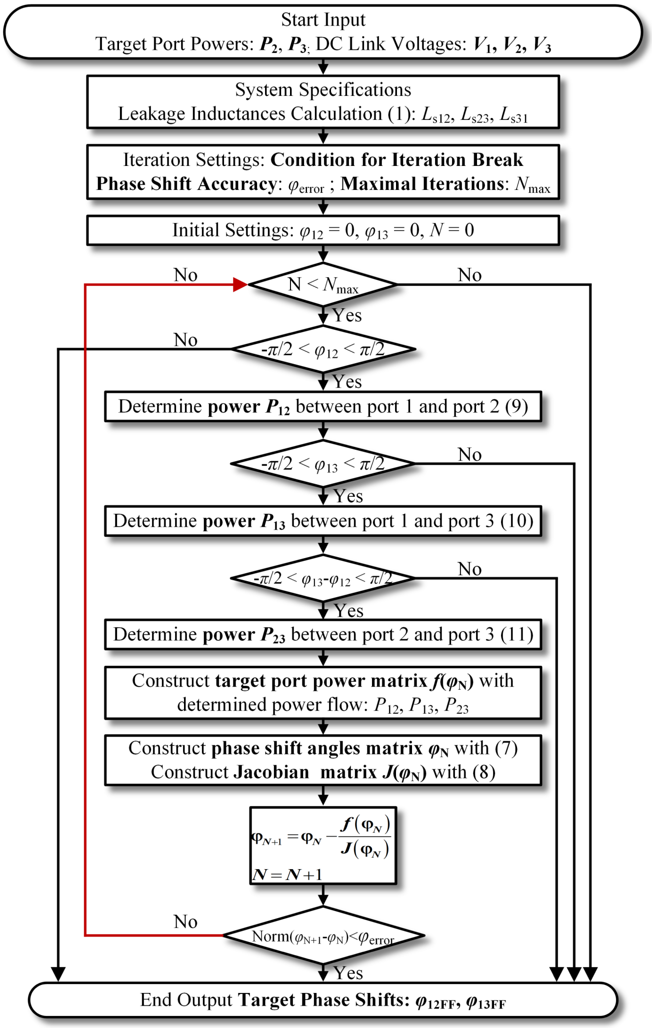

Fig. 4. Flowchart for the proposed FF algorithm.

## III. PROPOSED DECOUPLING NETWORK DESIGNS

### A. Control-to-Output Transfer Function of TAB Converter

The derivation of an accurate control-to-output transfer function is essential for the controller design and stability analysis to realize decoupling power flow control and highly dynamic response for a TAB converter. The reduced order model is most widely used in literature, and the fundamental frequency small signal model presented in [2] is adopted in this article, where the control-to-output small signal transfer function matrix of TAB

---

$$P_1 = \frac{V_1 V_2 N_{tr12} L_{s3} \cdot \left(\varphi_{12} - \varphi_{12}^2/\pi\right) + V_1 V_3 N_{tr13} L_{s2} \cdot \left(\varphi_{13} - \varphi_{13}^2/\pi\right)}{2\pi f_{sw}\left(L_{s1}L_{s2} + L_{s1}L_{s3} + L_{s2}L_{s3}\right)}$$

$$P_2 = \frac{-V_1 V_2 N_{tr12} L_{s3} \cdot \left(\varphi_{12} - \varphi_{12}^2/\pi\right) + V_2 V_3 N_{tr23} L_{s1} \cdot \left(\varphi_{23} - \varphi_{23}^2/\pi\right)}{2\pi f_{sw}\left(L_{s1}L_{s2} + L_{s1}L_{s3} + L_{s2}L_{s3}\right)}$$

$$P_3 = \frac{-V_1 V_3 N_{tr13} L_{s2} \cdot \left(\varphi_{13} - \varphi_{13}^2/\pi\right) - V_2 V_3 N_{tr23} L_{s1} \cdot \left(\varphi_{23} - \varphi_{23}^2/\pi\right)}{2\pi f_{sw}\left(L_{s1}L_{s2} + L_{s1}L_{s3} + L_{s2}L_{s3}\right)}. \tag{4}$$

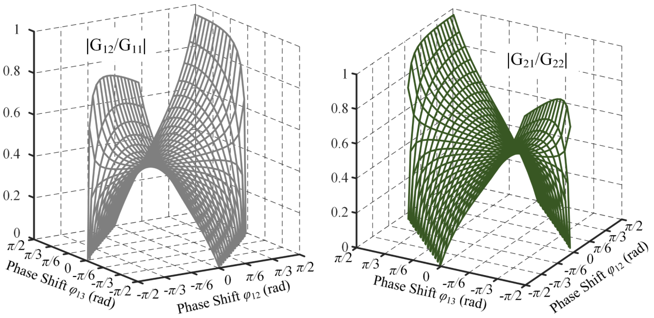

(a) (b)

Fig. 5. Intensity of cross-coupling between the interacted loops. (a) Interaction on the secondary side. (b) Interaction on the tertiary side.

converter can be represented as (12) and (13)

$$\tilde{i}_{\mathrm{dc2}} = G_{11} \cdot \tilde{\varphi}_{12} + G_{12} \cdot \tilde{\varphi}_{13} \tag{12}$$

$$\tilde{i}_{\mathrm{dc3}} = G_{21} \cdot \tilde{\varphi}_{12} + G_{22} \cdot \tilde{\varphi}_{13}. \tag{13}$$

Its fundamental frequency small signal model is defined as $G$ system matrix shown in (14)–(17), where $\phi_{12}$ and $\phi_{13}$ are the steady state value of phase shifts $\varphi_{12}$ and $\varphi_{13}$ on target point

$$G_{11} = \frac{-4}{\pi^3 f_{\mathrm{sw}} L_{s12}} V_1 \cos \phi_{12} - \frac{4}{\pi^3 f_{\mathrm{sw}} L_{s23}} V_3 \cos\left(\phi_{13} - \phi_{12}\right) \tag{14}$$

$$G_{12} = \frac{4}{\pi^3 f_{\mathrm{sw}} L_{s23}} V_3 \cos\left(\phi_{13} - \phi_{12}\right) \tag{15}$$

$$G_{21} = \frac{-4}{\pi^3 f_{\mathrm{sw}} L_{s23}} V_2 \cos\left(\phi_{13} - \phi_{12}\right) \tag{16}$$

$$G_{22} = \frac{-4}{\pi^3 f_{\mathrm{sw}} L_{s13}} V_1 \cos \phi_{13} - \frac{4}{\pi^3 f_{\mathrm{sw}} L_{s23}} V_2 \cos\left(\phi_{13} - \phi_{12}\right). \tag{17}$$

Therefore, the control-to-output small signal transfer function matrix of TAB converter is shown as follows:

$$\begin{bmatrix} \tilde{i}_{dc2} \\ \tilde{i}_{dc3} \end{bmatrix} = \begin{bmatrix} G_{11} & G_{12} \\ G_{21} & G_{22} \end{bmatrix} \cdot \begin{bmatrix} \tilde{\varphi}_{12} \\ \tilde{\varphi}_{13} \end{bmatrix}. \tag{18}$$

As shown in (12) and (13), from the control-to-output current small signal transfer function matrix of TAB converter, the reference variables of dc link current $i_{\mathrm{dc2}}$ and $i_{\mathrm{dc3}}$ are functions of both control variables $\varphi_{12}$ and $\varphi_{13}$, leading to an interaction between two control loops. The disturbance caused by the coupled term has a negative impact on the other control loop. For example, a positive increase in $\varphi_{12}$ will raise $i_{\mathrm{dc2}}$ through $G_{11}$, but simultaneously decreases $i_{\mathrm{dc3}}$ due to the coupled term $G_{21}$. To quantify the intensity of interaction among the control loops, the ratios "$|G_{12}/G_{11}|$" and "$|G_{21}/G_{22}|$" are used to evaluate the cross-coupling degree on the secondary side and the tertiary side, respectively. The intensity of cross-coupling between the interacted loops is shown in Fig. 5. As shown Fig. 5(a) and (b), the intensity of cross-coupling on each side varies significantly according to the operation conditions. The degree of cross-coupling is between [0, 1], indicating weak interaction at some operating points, but severe interference particularly under high power conditions. This increasing interaction at higher power levels poses challenges to the controllability and reliability of the TAB converter across the full power range.

Thus, an appropriate decoupling network design to decompose the interaction between the two current loops is essential for the independent control loop design. The issues associated with the decoupling network are usually solved by the diagonal matrix method [2]. In this work, two adaptive and highly dynamic decoupling approaches, i.e., the ideal decoupling method and the simplified decoupling method are proposed to eliminate the interaction between control loops with a designed compensation network. For comparison purpose, the conventional decoupling [2] is adopted as a baseline.

### B. Ideal Decoupling

Based on the cross-coupled control-to-output current small signal transfer function matrix $G_{ij}$ in (18), the proposed ideal decoupling is designed as shown in Fig. 6(a), which yields a desirable apparent process control loop [36], [37], the interacted system behaves as if the original interaction loops were not present by adding the ideal decoupling network.

The control variables of PI controller outputs are defined as the phase shift $\tilde{\varphi}'_{12}$ and $\tilde{\varphi}'_{13}$, the phase shift angles after decoupling network are defined as $\tilde{\varphi}_{12}$ and $\tilde{\varphi}_{13}$, the elements of ideal decoupling network are designed as follows:

$$\tilde{\varphi}_{12} = D_{11} \cdot \tilde{\varphi}'_{12} + D_{12} \cdot \tilde{\varphi}'_{13} \tag{19}$$

$$\tilde{\varphi}_{13} = D_{21} \cdot \tilde{\varphi}'_{12} + D_{22} \cdot \tilde{\varphi}'_{13}. \tag{20}$$

Combined with (12) and (13), the process equation from $\tilde{\varphi}'_{12}$ and $\tilde{\varphi}'_{13}$through the ideal decoupling network $D_{ij}$ and the coupled system network $G_{ij}$ to the reference variables $i_{\mathrm{dc2}}$ and $i_{\mathrm{dc3}}$ is shown as follows:

$$\begin{bmatrix} \tilde{i}_{dc2} \\ \tilde{i}_{dc3} \end{bmatrix} = \begin{bmatrix} G_{11} & G_{12} \\ G_{21} & G_{22} \end{bmatrix} \cdot \begin{bmatrix} D_{11} & D_{12} \\ D_{21} & D_{22} \end{bmatrix} \cdot \begin{bmatrix} \tilde{\varphi}'_{12} \\ \tilde{\varphi}'_{13} \end{bmatrix}. \tag{21}$$

That is

$$\begin{aligned} \tilde{i}_{dc2} = {} & (G_{11}D_{11} + G_{12}D_{21}) \cdot \tilde{\varphi}'_{12} + (G_{11}D_{12} \\ & + G_{12}D_{22}) \cdot \tilde{\varphi}'_{13} \end{aligned} \tag{22}$$

$$\begin{aligned} \tilde{i}_{dc3} = {} & (G_{21}D_{11} + G_{22}D_{21}) \cdot \tilde{\varphi}'_{12} + (G_{21}D_{12} \\ & + G_{22}D_{22}) \cdot \tilde{\varphi}'_{13}. \end{aligned} \tag{23}$$

According to (22) and (23), to eliminate the interaction between the reference variable currents $i_{\mathrm{dc2}}$ and $i_{\mathrm{dc3}}$, the process equation must satisfy the following ideal decoupling condition:

$$G_{11}D_{12} + G_{12}D_{22} = 0 \tag{24}$$

$$G_{21}D_{11} + G_{22}D_{21} = 0. \tag{25}$$

On the other hand, the apparent process transfer function (APTF) is set to guarantee that the system behaves as if there were no decoupling channels, i.e., the APTF is set to be like (26) and (27)

$$\tilde{i}_{dc2} / \tilde{\varphi}'_{12} = G_{11}D_{11} + G_{12}D_{21} = G_{11} \tag{26}$$

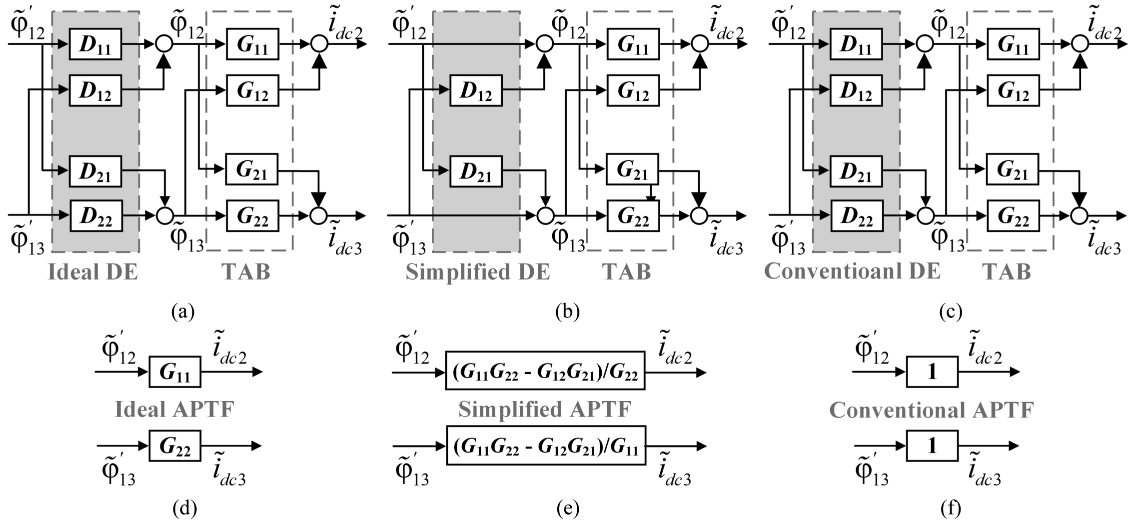

Fig. 6. Proposed decoupling methods. (a) Ideal decoupling. (b) Simplified decoupling. (c) Conventional decoupling (baseline [2]). (d) APTF of TAB with ideal decoupling. (e) APTF of TAB with simplified decoupling. (f) APTF of TAB with conventional decoupling.

$$\tilde{i}_{\text{dc3}}/\tilde{\varphi}'_{13} = G_{21}D_{12} + G_{22}D_{22} = G_{22}. \tag{27}$$

Obviously, from (26) and (27), the equivalent APTF process is shown in Fig. 6(d) after the ideal decoupling network applied on the TAB converter system.

In summary, combined with the ideal decoupling condition (24), (25) and APTF (26), (27), the ideal decoupling elements $D_{ij}$ can be solved as

$$D_{11} = \frac{G_{11}G_{22}}{G_{11}G_{22} - G_{12}G_{21}} \tag{28}$$

$$D_{12} = \frac{-G_{12}G_{22}}{G_{11}G_{22} - G_{12}G_{21}} \tag{29}$$

$$D_{21} = \frac{-G_{11}G_{21}}{G_{11}G_{22} - G_{12}G_{21}} \tag{30}$$

$$D_{22} = \frac{G_{11}G_{22}}{G_{11}G_{22} - G_{12}G_{21}}. \tag{31}$$

Although interaction loops are eliminated and the desirable APTF loop is achieved, there are still four complicated compensation elements. In addition, its performance is limited to being used for higher order system and highly nonlinear system [28].

For this reason, another decoupling approach, namely simplified decoupling, is proposed to implement the compensation network easily. Compared with the ideal decoupling method, simplified decoupling has less stringent requirements on the diagonal elements of the process. In other words, it does not emphasize much on what the primary loops become after decoupling. Instead, it assigns less task to the decoupler by setting the diagonal elements to be 1 [29].

### C. Simplified Decoupling

A straightforward decoupling method is proposed in this section to insert two compensators to cancel the direct effect of one manipulative variable by correctly changing the other manipulative variable [28]. The proposed simplified decoupling method is designed as shown in Fig. 6(b), which produces a simplified transfer function but yields a less-than-desirable apparent process [29]. Based on the process equation of ideal decoupling (22) and (23), if the decoupling elements $D_{11}$ and $D_{22}$ are assigned to be 1, i.e., the off-diagonal elements vanish. Then the process equation from $\tilde{\varphi}'_{12}$ and $\tilde{\varphi}'_{13}$through the simplified decoupling elements $D_{ij}$ and the coupled $G$ network to the reference variables $i_{\text{dc2}}$ and $i_{\text{dc3}}$ are shown as follows:

$$\begin{bmatrix} \tilde{i}_{\text{dc2}} \\ \tilde{i}_{\text{dc3}} \end{bmatrix} = \begin{bmatrix} G_{11} & G_{12} \\ G_{21} & G_{22} \end{bmatrix} \begin{bmatrix} 1 & D_{12} \\ D_{21} & 1 \end{bmatrix} \begin{bmatrix} \tilde{\varphi}'_{12} \\ \tilde{\varphi}'_{13} \end{bmatrix}. \tag{32}$$

Namely

$$\tilde{i}_{\text{dc2}} = (G_{11} + G_{12}D_{21}) \cdot \tilde{\varphi}'_{12} + (G_{11}D_{12} + G_{12}) \cdot \tilde{\varphi}'_{13} \tag{33}$$

$$\tilde{i}_{\text{dc3}} = (G_{21} + G_{22}D_{21}) \cdot \tilde{\varphi}'_{12} + (G_{21}D_{12} + G_{22}) \cdot \tilde{\varphi}'_{13}. \tag{34}$$

Based on (33) and (34), the following conditions are set to satisfy the simplified decoupling network requirement:

$$G_{11}D_{12} + G_{12}D_{22} = 0 \tag{35}$$

$$G_{21}D_{11} + G_{22}D_{21} = 0. \tag{36}$$

Thus, the decoupling elements $D_{12}$ and $D_{21}$ of simplified decoupling can be solved as follows:

$$D_{12} = -G_{12}/G_{11} \tag{37}$$

$$D_{21} = -G_{21}/G_{22}. \tag{38}$$

Therefore, the APTF of simplified decoupling is dereived as follows, which is shown in Fig. 6(e):

$$\tilde{i}_{\text{dc2}}/\tilde{\varphi}'_{12} = (G_{11}G_{22} - G_{12}G_{21})/G_{22} \tag{39}$$

$$\tilde{i}_{\text{dc3}}/\tilde{\varphi}'_{13} = (G_{11}G_{22} - G_{12}G_{21})/G_{11}. \tag{40}$$

Compared to the ideal decoupling network shown in (28)–(31), the simplified decoupling network as shown in (37) and

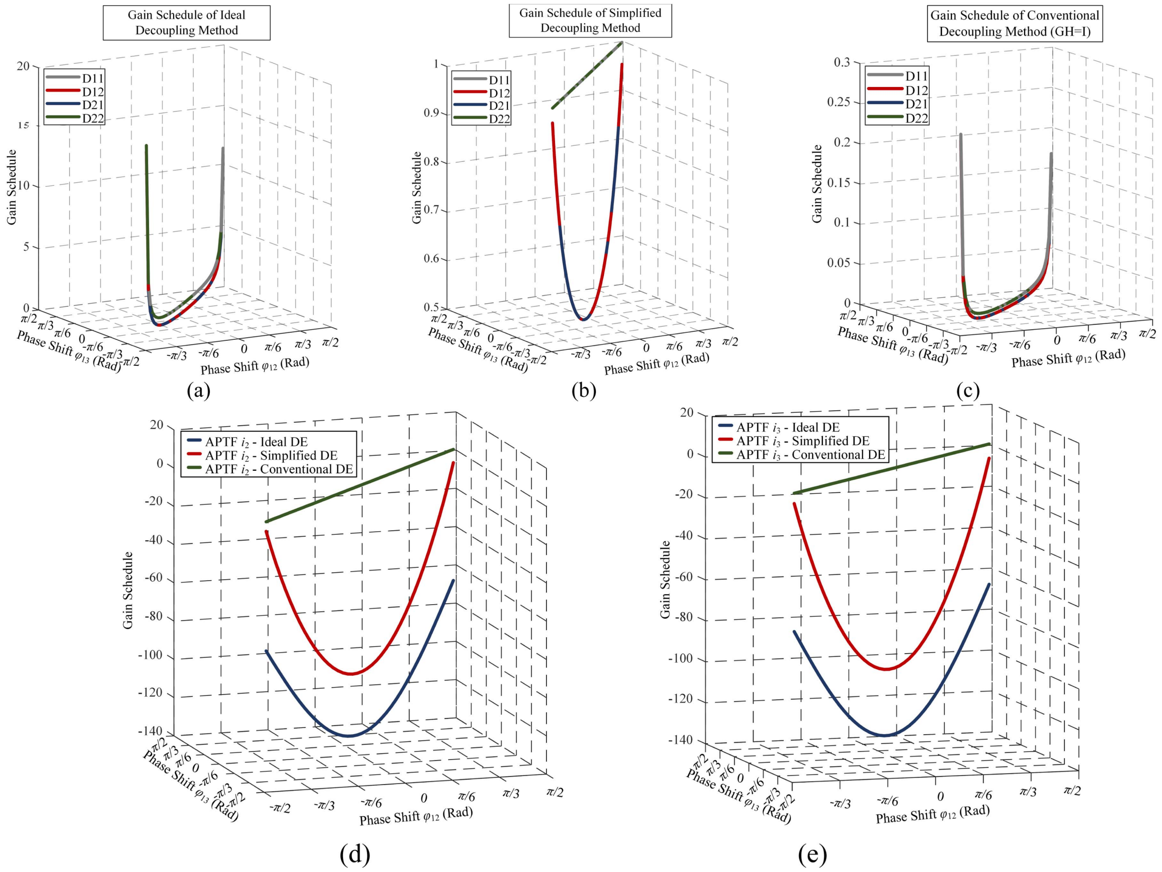

(a) (b) (c)

(d) (e)

Fig. 7. Gain schedule of diverse decoupling methods. (a) Ideal decoupling. (b) Simplified decoupling. (c) Conventional decoupling (baseline). (d) APTF comparison of $i_2$. (e) APTF comparison of $i_3$.

(38) has less stringent requirements on the diagonal elements of the process. It assigns less task to the decoupler by setting the diagonal elements to be 1.

Using these two proposed highly dynamic decoupling methods, the original coupled power loop of $i_{\mathrm{dc}2}$ and $i_{\mathrm{dc}3}$ are decoupled, the closed-loop controller with independent power regulation of each port in the TAB converter can be designed.

### D. Conventional Decoupling

The most used decoupling network design for a TAB converter was presented in [2]. Its decoupling elements are determined based on $GD = \mathrm{diag}$ [1], [1], as shown in Fig. 6(c). Similarly, its APTF process equation is shown as follows:

$$\begin{aligned}\tilde{i}_{\mathrm{dc}2} = {} & (G_{11}D_{11} + G_{12}D_{21}) \cdot \tilde{\varphi}'_{12} + (G_{11}D_{12} \\ & + G_{12}D_{22}) \cdot \tilde{\varphi}'_{13}\end{aligned} \tag{41}$$

$$\begin{aligned}\tilde{i}_{\mathrm{dc}3} = {} & (G_{21}D_{11} + G_{22}D_{21}) \cdot \tilde{\varphi}'_{12} + (G_{21}D_{12} \\ & + G_{22}D_{22}) \cdot \tilde{\varphi}'_{13}.\end{aligned} \tag{42}$$

From (43), obviously, the control-to-output transfer function of any TAB converter is a unit gain schedule without any system information, which presents a challenge for the system evaluation and controller design

$$\begin{aligned}\tilde{i}_{\mathrm{dc}2}/\tilde{\varphi}'_{12} &= 1 \\ \tilde{i}_{\mathrm{dc}3}/\tilde{\varphi}'_{13} &= 1.\end{aligned} \tag{43}$$

### E. Gain Schedule Comparison of Different Decoupling Network

As shown in Fig. 7, the conventional decoupling control method is designed to be a fixed unit gain schedule system no matter what kind of TAB converter and operation points, it cannot adapt to the real system. However, the proposed ideal and simplified decoupling control methods are adaptive decoupling network to varying system operations.

In numeric analysis, the introduced decoupling methods differ mainly in the way manipulating interaction loops. Fig. 7 gives the steady state gains [$D_{11}$, $D_{12}$, $D_{21}$, $D_{22}$] of proposed ideal, simplified and conventional decouplers. As shown in Fig. 7(a), the gain schedules of ideal decouplers range from 1.0 to 15, the simplified decouplers' gain schedules are within the range of [0.5, 1] shown in Fig. 7(b), but the gains of the conventional decouplers are obviously smaller to the range of [0, 0.2] as shown in Fig 6(c). Since the TAB converter has the same leakage inductances and other system specifications for simplicity in this work, thus, the decoupling elements $D_{11}$ and $D_{12}$ are also symmetric with $D_{21}$ and $D_{22}$, as shown in Fig. 7(a)–(c). The

TABLE III
COMPARISON OF DECOUPLING ELEMENTS IN DIFFERENT DECOUPLING METHODS

| Decoupling Methods | Ideal Decoupling | Simplified Decoupling | Conventional Decoupling |
|---|---|---|---|
| **Apparent Process Function $G_{\mathrm{APTF}}(s)$** | $G_{i2/\tilde{\varphi}'_{12}}(s) = \frac{\tilde{i}_2}{\tilde{\varphi}'_{12}} = G_{11}$<br>$G_{i3/\tilde{\varphi}'_{13}}(s) = \frac{\tilde{i}_3}{\tilde{\varphi}'_{13}} = G_{22}$ | $G_{i2/\tilde{\varphi}'_{12}}(s) = \frac{\tilde{i}_2}{\tilde{\varphi}'_{12}} = \frac{G_{11}G_{22} - G_{12}G_{21}}{G_{22}}$<br>$G_{i3/\tilde{\varphi}'_{13}}(s) = \frac{\tilde{i}_3}{\tilde{\varphi}'_{13}} = \frac{G_{11}G_{22} - G_{12}G_{21}}{G_{11}}$ | $G_{i2/\tilde{\varphi}'_{12}}(s) = 1$<br>$G_{i3/\tilde{\varphi}'_{13}}(s) = 1$ |
| **Decoupling Elements** | $D_{11} = \frac{G_{22}G_{11}}{G_{11}G_{22} - G_{12}G_{21}}$<br>$D_{12} = \frac{-G_{12}G_{22}}{G_{11}G_{22} - G_{12}G_{21}}$<br>$D_{21} = \frac{-G_{21}G_{11}}{G_{11}G_{22} - G_{12}G_{21}}$<br>$D_{12} = \frac{G_{11}G_{22}}{G_{11}G_{22} - G_{12}G_{21}}$ | $D_{11} = 1$<br>$D_{12} = \frac{-G_{12}}{G_{11}}$<br>$D_{21} = \frac{-G_{21}}{G_{22}}$<br>$D_{22} = 1$ | $D_{11} = \frac{G_{22}}{G_{11}G_{22} - G_{12}G_{21}}$<br>$D_{12} = \frac{-G_{12}}{G_{11}G_{22} - G_{12}G_{21}}$<br>$D_{21} = \frac{-G_{21}}{G_{11}G_{22} - G_{12}G_{21}}$<br>$D_{12} = \frac{G_{11}}{G_{11}G_{22} - G_{12}G_{21}}$ |

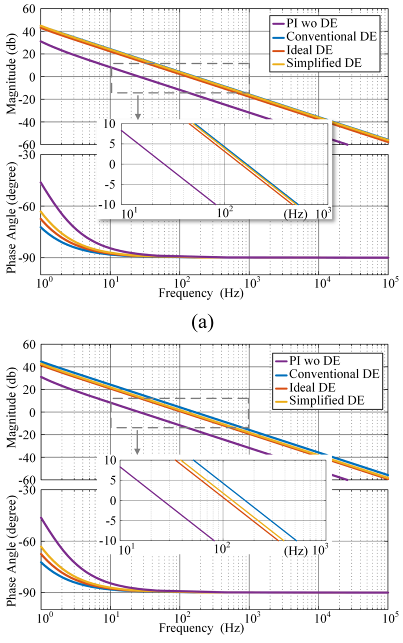

(a)

(b)

Fig. 8. Frequency response comparison with open loop Bode plots of current control loops with different decoupling networks. (a) A $\varphi_{12} = 0.2$ and $\varphi_{13} = 0.2$. (b) B $\varphi_{12} = 0.06$ and $\varphi_{13} = 0.26$.

gain schedules of ideal, simplified, and conventional decoupling methods are significantly different from each other from the orders of magnitude, which means that the decoupling network responds very differently to the same controller. Obviously, the conventional decoupling network has the slowest dynamic response as seen from its gain schedules, which is also been proved in the experimental study. Obviously, the gains of two proposed methods are not deviated too much, but the gains of conventional decoupling method show a relatively huge difference with very small gains, which slow down the TAB's dynamic response speed significantly.

The APTF of different decoupling methods is shown in Fig. 7(d) and (e). The corresponding controllers of the TAB converter are highly dependent on its APTF. Because the APTF of the conventional decoupling method is fixed to a unit gain schedule, but the APTF of the proposed methods is adaptive to the operation points of the system. Thus, the proposed methods can adapt to the system's operation to improve its dynamic performance, especially across the entire power range.

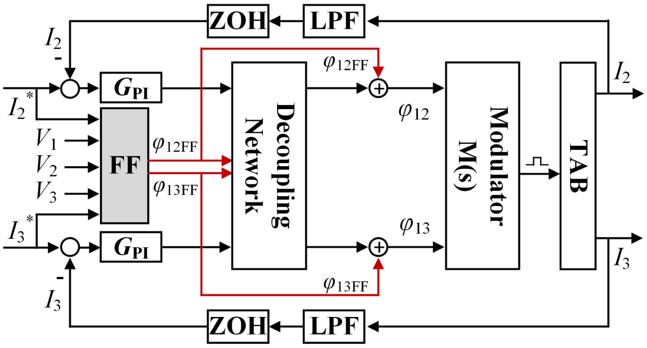

Fig. 9. Decoupling control diagram of TAB converter.

## F. Frequency Response Analysis

In the controller architecture of the TAB converter, there are two independent current control loops as shown in Fig. 9. The frequency response function FRF(s) of the system is calculated according to (44) using the open loop transfer functions: apparent process transfer function $G_{\mathrm{APTF}}(s)$ shown in Table III, PI controller $G_{\mathrm{PI}}(s)$, output capacitor function $G_{\mathrm{cap}}(s)$. Since the TAB converter studied in this work is symmetric, only the secondary port's FRF(s) with different decoupling methods is given for comparison and analysis for simplicity

$$\mathrm{FRF}(s) = G_{\mathrm{PI}}(s) \cdot G_{\mathrm{APTF}}(s) \cdot G_{\mathrm{cap}}(s). \tag{44}$$

The theoretical open loop Bode plots of the current control loop for secondary port are illustrated in Fig. 8. As shown in Fig. 8(a), the operating phase shifts $\varphi_{12}$ and $\varphi_{13}$ are set to be the same with operation point A. To make a fair comparison between the different control methods, each controller is optimized to have the same dynamic performance. Except for the single PI control method, the conventional decoupling control has been optimized in the same way as the proposed decoupling control. Thus, the conventional decoupling control and the proposed decoupling controls can achieve similar dynamic performance at

TABLE IV
SPECIFICATIONS OF EXPERIMENTAL TAB CONVERTER

| | |
|---|---|
| DC port's voltages | $V_1 = V_2 = V_3 = 300$ V |
| Switching frequency | $f_{sw} = 10$ kHz |
| Leakage inductances $L_{si}$ | $L_{s1} = L_{s2} = L_{s3} = 20\ \mu$H |
| DC link capacitances | $C_1 = C_2 = C_3 = 390\ \mu$F |
| Transformer turns ratio | $n_1 : n_2 : n_3 = 1 : 1 : 1$ |
| Maximum tested power | 9 kW |
| Deadtime | 2 $\mu$s |
| DSP Controller | TMS320F28379D |
| SiC MOSFET | HT-3234-R-VB (Wolfseed) |

the operating point A [0.2, 0.2]. The crossover frequency is 231 Hz for the conventional decoupling control and the proposed decoupling control. Because of the nonlinearity and cross-coupling issue of TAB converter, the single PI control cannot be optimized in the same way as the TAB with decoupling network. Thus, its crossover frequency is set to 36.7 Hz, resulting in a slow transient response but staying stable across the entire power range of TAB converter.

However, the system model of TAB converter varies across the full power range. Fig. 8(b) demonstrates the controllers of different methods at another operating point B [0.06, 0.26]. Similarly, the single PI control and conventional decoupling control remain the same as the one at A [0.2, 0.2]. But the crossover frequencies of proposed ideal decoupling control and simplified decoupling control are adapted to 154 Hz and 174 Hz, respectively. Obviously, the comparison between Fig. 8(a) and (b) reveals that the controllers with proposed decoupling methods are adaptive according to the operation points of TAB converter, while the controller with conventional decoupling network remains the same at different operation points and even in different TAB applications. The controllers employing adaptive equivalent decoupling networks ensure highly dynamic performance and controllability across the entire power range of the TAB converter.

### G. Decoupling Control Strategy Design

The overall control block diagram to implement the decoupling network for TAB converter is shown in Fig. 9, where the duty cycles $d_1$, $d_2$, and $d_3$ are all set to be 0.5. Since the small signal transfer function based system gain matrix $G$ is derived from the phase shifts of real-time target operation point, thus, the real-time updated system matrix $G$ is realized through the proposed FF block for target operating phase shifts calculation. The decoupling network combines with the FF network to eliminate the cross coupling between two control loops as the proposed decoupling control strategy.

## IV. EXPERIMENTAL VALIDATION FOR DECOUPLING CONTROL

The test setup shown in Fig. 10 was used to validate the effectiveness of proposed decoupling control methods for the TAB converter. As shown in Table IV, the leakage inductances of $L_{s1}$, $L_{s2}$, and $L_{s3}$ are 20 $\mu$H and the switching frequency is 10 kHz in this study. The experiments are carried out in pump-back configuration to circulate higher power with limited dc power supply. Because the test is adopted in pump-back configuration, the dc output currents $I_2$ and $I_3$ are selected as control variable, and the dc port voltage $V_1$, $V_2$, and $V_3$ are set to be constant 300 V in tests. Similar current control loops have been studied also in [2] as a general control method for TAB converter, as well as its application in TAB-based SST system, charge station, and PV system. The direction of dc port currents $I_1$, $I_2$, and $I_3$ shown in Fig. 1 is defined as positive from the converter to the transformer. The controller used in this work is the TMS320F28379D.

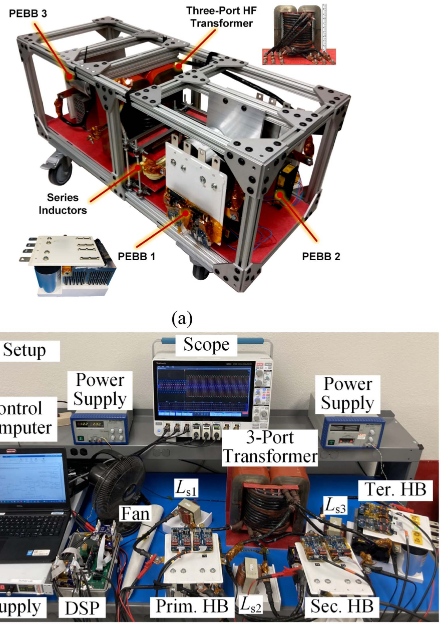

(a)

(b)

Fig. 10. Hardware for experimental study. (a) Packaged TAB prototype. (b) Test setup.

### A. Proposed FF Validation

To validate the effectiveness of the proposed FF algorithm in calculating the target operating phase shift angles based on the desired ports' power. Given that the desired dc ports' power $P_1$, $P_2$, $P_3$ and voltages $V_1$, $V_2$, $V_3$ as the input of the proposed FF loop, the simulation outputs of the proposed FF loop, namely the phase shift angles $\varphi_{12}$ and $\varphi_{13}$, are adopted to fit the known power versus phase shifts relationship curve as shown in Fig. 3.

For simplicity, the dc ports' voltages are set to be 300 V. As shown in Fig. 11, the output of the proposed FF loop at the secondary port and tertiary port is indicated in green with "$*$" and in red with "$\Delta$," respectively. Judging from the matching results, the output results basically fit the known power versus phase shifts relationship curve correctly. In practice, the losses and sampling errors can affect the output accuracy of the proposed FF loop. Thus, advanced power models of TAB converters can further improve the accuracy of the proposed FF loop.

### B. Effectiveness Validation: A to B

The experimental results shown in Figs. 12–16 are used for the comparison between the test without decoupling (M1), the

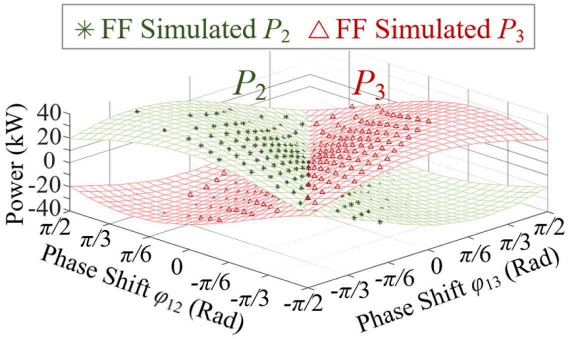

Fig. 11. Simulation output of the proposed FF loop.

TABLE V
OPERATING POINTS FOR DECOUPLING CONTROL VALIDATION

| Specification | Operation Points ($V_1 = V_2 = V_3 = 300$ V) | | |
|---|---|---|---|
| | A | B | C |
| $I_1$ (A) | +20.42 | +19.93 | +1.12 |
| $I_2$ (A) | -9.67 | -29.58 | -30.05 |
| $I_3$ (A) | -9.93 | +11.01 | +30.52 |
| $\varphi_{12}$ (rad) | +0.195 | +0.151 | 0.139 |
| $\varphi_{13}$ (rad) | +0.312 | +0.067 | -0.17 |
| $P_1$ (kW) | +6.126 | +5.980 | +0.336 |
| $P_2$ (kW) | -2.9 | -8.874 | -9.015 |
| $P_3$ (kW) | -2.98 | +3.3 | +9.156 |
| Efficiency | 0.96 | 0.96 | 0.95 |
| ZVS | ZVS | ZVS | ZVS |

test with conventional decoupling (M2), the test with ideal decoupling (M3) and the test with simplified decoupling (M4), the tested operation points A and B of steady state are given in Table V. There are two groups of contrast experiments with step command change from A to B in Fig. 12 and from B to A in Figs. 13 and 14.

Fig. 12 is presented to validate the effectiveness of the proposed decoupling control methods, the controllers of the test without decoupling, the test with conventional decoupling, the test with ideal decoupling and simplified decoupling are optimized for the experiment from operation point A to operation point B, respectively. The optimization of all tested control methods is targeted to have the same dynamic response performance. All the tests are implemented under the same condition, the only difference is the decoupling network. The dynamic performance of dc port currents $i_1$ (blue), $i_2$ (green), and $i_3$ (red) are adopted to analyze and compare the effectiveness of proposed decoupling methods. From A to B, the secondary current $i_2$ is stepped up from $-9.67$ to $-29.58$ A, the tertiary current $i_3$ is inversed from $-9.93$ to $+11.01$ A, while the primary current $i_1$ is kept same $+20$ A.

To make a fair comparison of the response times of different control methods M1–M4, *the same maximum overshoots are set*, as shown in Fig. 12(a1), (b), (c), and (d), respectively. As shown in Fig. 12(a1), for the test using a PI controller without decoupling, although its overshoots are minimized to $[|\Delta I_{1,\max}| = 0.6$ A, $|\Delta I_{2,\max}| = 0$ A, $|\Delta I_{3,\max}| = 0$ A], its response time increases to 6.46 ms. As studied in Section III, given a known system model, the conventional decoupling network can be optimized to match the proposed ideal or simplified decoupling network, achieving the same dynamic performance, as illustrated in Fig. 6 and Table III. Accordingly, the test with conventional decoupling control is optimized to be equivalent to the proposed ideal decoupling by integrating the system model $G_{11}$ on the secondary side and $G_{22}$ on the tertiary side. For the tests using conventional decoupling, proposed ideal decoupling, and simplified decoupling as shown in Fig. 12(b)–(d), respectively, the corresponding three tests show similar dynamic performance. Obviously, its response time is significantly improved once the optimized decoupling control is applied. The test with conventional decoupling control is shown in Fig. 12(b) and the test with proposed ideal decoupling control is shown in Fig. 12(c), the response time is similarly improved to 1.68 ms, while the maximum overshoots are similarly minimized to $[|\Delta I_{1,\max}| = 1.2$ A, $|\Delta I_{2,\max}| = 0$ A, $|\Delta I_{3,\max}| = 0.0$ A]. This is because the conventional decoupling control has been optimized to achieve the same dynamic performance as the proposed decoupling control. After the simplified decoupling applied as shown in Fig. 12(d), similar maximum overshoots are observed at $[|\Delta I_{1,\max}| = 1.5$ A, $|\Delta I_{2,\max}| = 0$ A, $|\Delta I_{3,\max}| = 0.0$ A], while the response time is also improved to 1.68 ms.

To compare the overshoots of different control methods M1–M4 under the same response time, the response time is set to 1.68 ms for all tests, as shown in Fig. 12(a2), (a3), (b), (c), and (d), respectively. As shown in Fig. 12(a2), when attempting to improve the response time of the PI controller without decoupling, the resulting overshoots become significantly larger, reaching $[|\Delta I_{1,\max}| = 3.5$ A, $|\Delta I_{2,\max}| = 5.3$ A, $|\Delta I_{3,\max}| = 8.2$ A]. Even so, its response time remains limited to 4.76 ms. Due to the inherent interaction and nonlinearity of the TAB converter, highly dynamic control cannot be achieved using PI control alone. Thus, the test with FF but without decoupling control shown in Fig. 12(a3) is adopted to set the same response time 1.68 ms for overshoots comparison. As shown in Fig. 12(a3), the overshoots of the test with FF but without decoupling control reach to $[|\Delta I_{1,\max}| = 1.6$ A, $|\Delta I_{2,\max}| = 3.1$ A, $|\Delta I_{3,\max}| = 5.8$ A]. After the decoupling network is applied to the TAB converter, its overshoots are significantly reduced to near zero for the test using conventional decoupling as shown in Fig. 12(b), proposed ideal decoupling as shown in Fig. 12(c), and simplified decoupling as shown in Fig. 12(d), while maintaining the same response time of 1.68 ms. Obviously, the TAB converter can achieve highly dynamic performance while maintaining low overshoots among different dc current ports when using decoupling control methods.

In summary, oscillations are observed in $i_2$ and $i_3$ in the case without decoupling control (M1). To validate the effectiveness of the proposed decoupling control methods, all controllers are separately optimized from A to B. Thus, similar dynamic performance is realized for the tests with conventional decoupling (M2), proposed ideal decoupling (M3), and simplified decoupling (M4). These results further verify the effectiveness of the proposed decoupling strategies and demonstrate that highly dynamic control cannot be realized without decoupling in TAB converters.

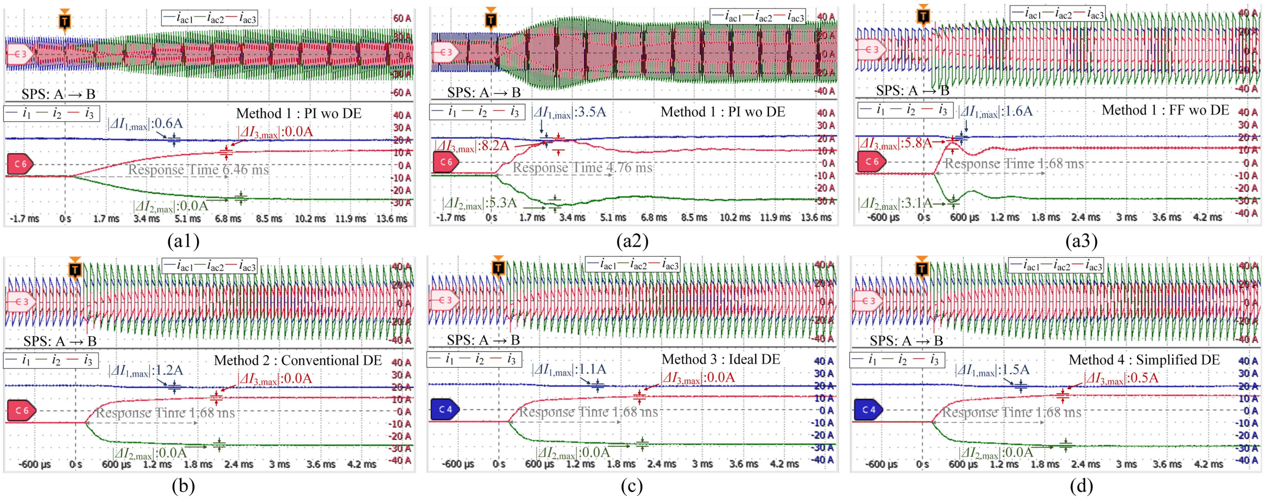

(a1) (a2) (a3)
(b) (c) (d)

Fig. 12. Experimental results for decoupling comparison from operating point A to B. (a1) Method 1: slow PI without decoupling. (a2) Method 1: fast PI without decoupling. (a3) Method 1: FF without decoupling. (b) Conventional decoupling. (c) Ideal decoupling. (d) Simplified decoupling.

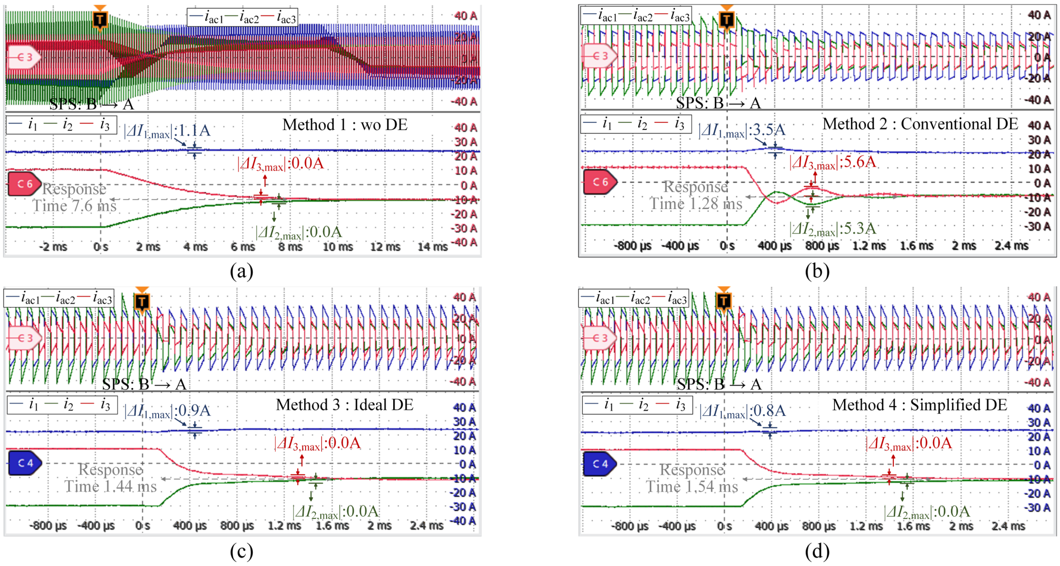

(a) (b)
(c) (d)

Fig. 13. Experimental results for decoupling comparison from operating point B to A. (a) PI without decoupling. (b) With conventional decoupling. (c) With ideal decoupling. (d) With simplified decoupling.

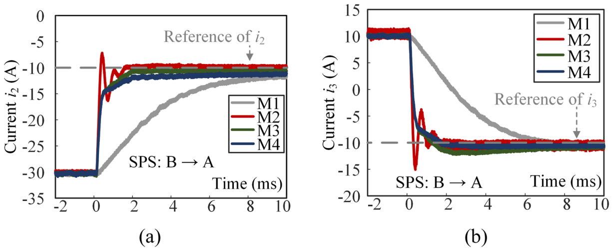

(a) (b)

Fig. 14. Overshoots and dynamic comparison between different decoupling methods from B to A. (a) Comparison of $i_2$. (b) Comparison of $i_3$.

### C. Adaptiveness Validation: B to A

As shown in Fig. 12, the controllers for tests with different decoupling methods are optimized for the transition from operating point A to B, and the tests with conventional decoupling and proposed decoupling methods show similar dynamic performance. To validate the adaptive feature of the proposed decoupling methods, the same optimized controllers are adopted for the test from operation point B to A, while the dc voltages are still set to be 300 V.

The tests from B to A shown in Fig. 13 are presented to validate the adaptive feature of proposed decoupling control methods compared to the controllers without decoupling and with conventional decoupling. All controllers remain the same optimized for the experiment from operation point A to B. From B to A, the secondary current $i_2$ is stepped down from $-29.58$ to $-9.67$ A, the tertiary current $i_3$ is inversed from $+11.01$ to $-9.93$ A, while the primary current $i_1$ is maintained around 20 A.

Obviously, for the test with PI controller but without decoupling (M1) as shown in Fig. 13(a), its overshoots are close to

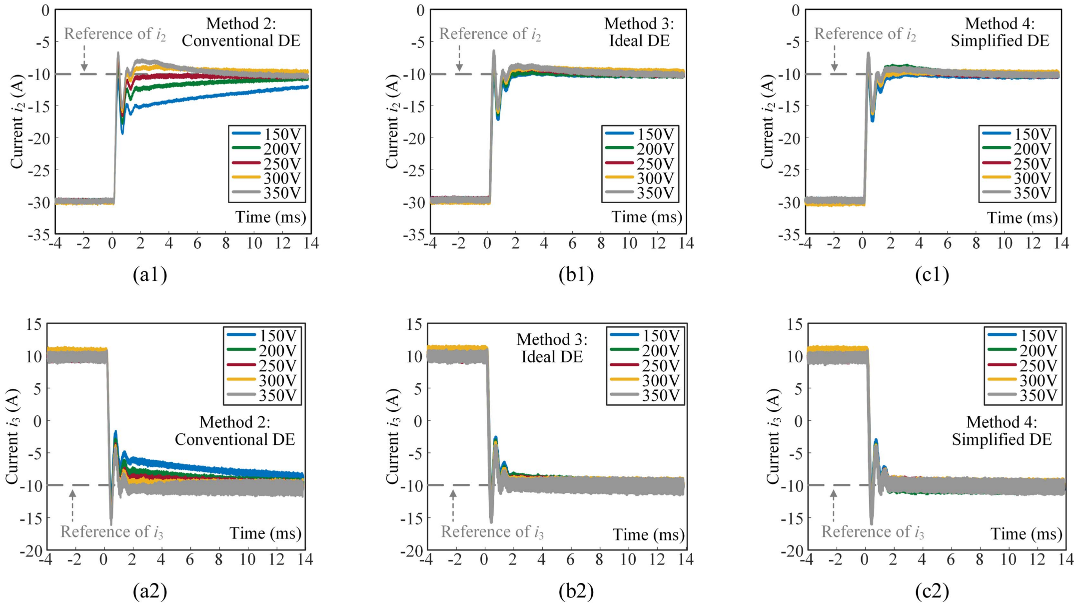

Fig. 15. Experimental results for decoupling comparison from operating point B to A with varying DC voltages. (a1) Comparison of $i_2$ with conventional decoupling. (a2) Comparison of $i_3$ with conventional decoupling. (b1) Comparison of $i_2$ with ideal decoupling. (b2) Comparison of $i_3$ with ideal decoupling. (c1) Comparison of $i_2$ with simplified decoupling. (c2) Comparison of $i_3$ with simplified decoupling.

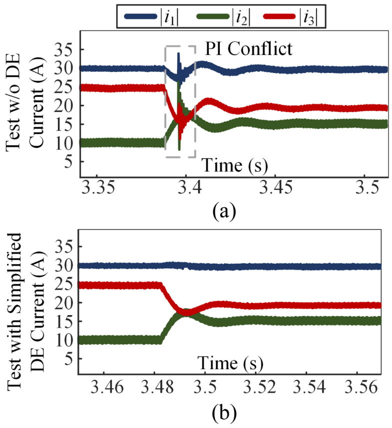

Fig. 16. Tests for controller robust comparison. (a) Test without decoupling. (b) Test with simplified decoupling.

zero, but its response time reaches 7.6 ms. Moreover, for the test with conventional decoupling control (M2) as shown in Fig. 13(b), its overshoots are [$|\Delta I_{1,\max}| = 3.5$A, $|\Delta I_{2,\max}| = 5.3$ A, $|\Delta I_{3,\max}| = 5.6$ A], while its response time is reduced to 1.28 ms. However, the dynamic performance of conventional decoupling control degrades, when operation condition of TAB converter is changed but its controller is not adaptively adjusted.

In contrast, the proposed ideal decoupling and simplified decoupling as shown in Fig. 13(c) and (d), its response times are 1.44 ms and 1.54 ms, respectively, while its maximum overshoots are significantly reduced to [$|\Delta I_{1,\max}| = 0.9$ A, $|\Delta I_{2,\max}| = 0.0$ A, $|\Delta I_{3,\max}| = 0.0$ A] and [$|\Delta I_{1,\max}| = 0.8$ A, $|\Delta I_{2,\max}| = 0.0$ A, $|\Delta I_{3,\max}| = 0.01$ A], respectively. In addition to the similar response time are achieved for conventional decoupling control (1.28 ms), proposed ideal decoupling control (1.44 ms) and simplified decoupling control (1.54 ms), the dynamic overshoots of TAB are obviously being smaller for proposed decoupling control methods.

Although the conventional decoupling controller is optimized at the test from A to B based on the proposed ideal decoupling's APTF function, the fixed controller cannot achieve equivalent dynamic performance as the proposed decoupling control methods at different operation from B to A. However, the proposed decoupling control methods can adaptively adjust to varying operation conditions, achieving consistently improved dynamic performance.

To clearly show the difference in dynamic performance of the dc port's currents, Fig. 14 extracts the dc port's currents from Fig. 13 for the test without decoupling control, the test with proposed ideal and simplified decoupling control, as well as conventional decoupling control for comparison. Although the oscillations can be controlled very small in the case with slow PI, particularly in $i_2$ and $i_3$, it sacrifices the response time. However, simply increasing the response time will lead to excessive overshoot and degraded controllability. This indicates that the system without decoupling control may suffer from poor dynamic performance and even potential instability. While conventional decoupling improves dynamic behavior to some extent, it cannot maintain consistent performance across varying operating conditions. The proposed decoupling control methods, however, effectively suppress overshoots and respond quickly, enabling highly dynamic operation under different conditions. Overall, Fig. 14 highlights that the proposed decoupling control methods "ideal decoupling" and "simplified decoupling" can adaptively improve the dynamic performance of the TAB converter.

### *D. Adaptiveness Validation: B to A With Different DC Voltages*

To further validate the adaptive feature of the proposed decoupling methods under varying dc port voltage, the comparison tests are adopted for the test with the conventional decoupling control method (M2), test with proposed ideal decoupling control method (M3) and the simplified decoupling control method (M4). Similarly, the tests are conducted from operation point B to A, but the dc voltages vary from 150 to 350 V. The controllers are identically optimized from operation point B to A at the dc voltage 300 V.

Fig. 15(a)–(c) shows the tests with different control methods from B to A at dc voltage 300 V, and the controllers are optimized to achieve the same dynamic performance, respectively. To verify the adaptive feature of the proposed decoupling control methods, the dc voltages are changed from 150 to 350 V. From Fig. 15(a1) and (a2) for the test with conventional decoupling control method, although similar dynamic performance can be achieved as the test with proposed decoupling control methods at the dc voltage 300 V, because the controllers are same optimized at 300 V, the overshoots of dc currents are increasing while the dc voltages increase to 350 V. Moreover, the dynamic response is slow when the dc voltage drops from 300 to 150 V. Because the APTF of the conventional decoupling method is fixed over the full power range of TAB converter, as shown in Figs. 6 and 7. For the proposed ideal decoupling control shown in Fig. 15(b1) and (b2) and the proposed simplified decoupling control shown in Fig. 15(c1) and (c2), the dynamic performance of dc currents $i_2$ and $i_3$ are keeping the similar fast response without sacrificing overshoot performance while the dc voltage varies from 150 to 350 V. Especially, the same optimized dynamic response is keeping at 1.6 ms when the dc voltage drops from 300 to 150 V.

The comparison shown in Fig. 15 confirms the effectiveness and adaptiveness of the proposed decoupling control methods in stabilizing the system and improving the dynamic performance of the system without sacrificing its dynamic response time and overshoot compared to control with the conventional decoupling method.

### *E. Robustness of Proposed Decoupling Method Validation*

Fig. 16 presents the comparison of the robust characteristic of TAB with the proposed decoupling design and without the decoupling design. Compared to the PI controller of tests in Fig. 12, its parameters are increased to verify the robust capability, the leakage inductances of $L_{s1}$, $L_{s2}$, and $L_{s3}$ are increased to 100 $\mu$H, and the switching frequency is increased to 20 kHz. As shown in Fig. 16(a), oscillation occurred during the load transient for the controller without decoupling, when the tertiary port current $i_3$ stepped up from 10 to 15 A and the primary port current $i_1$ is tracked its reference 30 A. However, the same experiment is implemented under the simplified decoupling network shown in Fig. 16(b), oscillations were eliminated during the transient. Based on the comparison in Fig. 16, the test without decoupling control exhibits significant oscillations and tends to become unstable. In contrast, the test with the proposed decoupling control demonstrates greater robustness, with a sufficient margin in the PI controller. This improvement is attributed to the fact that the proposed decoupling method manipulates the control variables of the TAB in a more rational and effective manner.

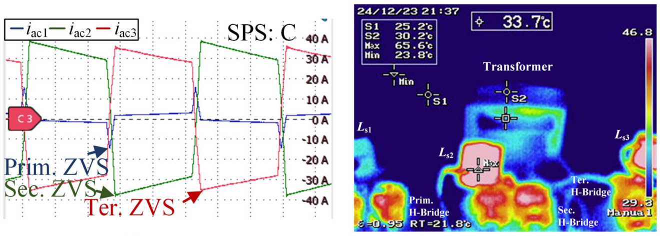

(a) (b)

Fig. 17. Test of operating point C. (a) Zoom-in view of operating point C with ZVS switching. (b) Thermal picture of operating point C.

TABLE VI
EXPERIMENTAL COMPARISON OF TAB'S DECOUPLING STRATEGIES

| Methods | Dynamic | Overshoot | Robust | Adaptive | Complexity |
|---|---|---|---|---|---|
| M1 | Bad | Bad | Bad | No | Simple |
| M2 | Moderate | Moderate | Moderate | No | Medium |
| M3, M4 | Good | Good | Good | Yes | Medium |

M1: wo DE; M2: Conventional DE; M3 and M4: Proposed DE

### *F. TAB Converter Prototype Validation*

The test at operation point C is shown in Fig. 17 with detailed ZVS switching analysis and thermal picture of TAB converter. The specification of operation point C is shown in Table V. The maximum power tested at operation point C is 9.49 kW, the primary, secondary, and tertiary devices are switched with ZVS, as shown in Fig. 17(a), and its efficiency reaches 95%. As shown in Fig. 17(b), the temperature of the prototype is measured in the primary leakage inductor with 33.7 °C, secondary and tertiary leakage inductors reach 65 °C, because the primary leakage inductor delivers more power to the secondary and tertiary port. The temperature of the transformer is measured at 38.8 °C. With increasing test power, the proposed decoupling methods help to improve the reliability of the TAB systems.

In summary, both proposed ideal decoupling and simplified decoupling networks work stably and effectively to mitigate the interaction between the two control loops of TAB converter, both decoupling designs can reduce the overshoot during transients and achieve faster dynamic response, which obviously improve the dynamic performance of TAB converter. The overall comparison of the different decoupling methods is also shown in Table VI. The system with proposed decoupling network is adaptive and robust, which can provide more design margin to TAB converter.

## V. CONCLUSION

In this article, novel decoupling control methods are proposed to address the cross-coupling issue in TAB converters. The proposed methods effectively reduce the power flow's oscillations without compromising the system's dynamic response speed. Moreover, the proposed methods adapt to varying operating points and dc voltages, significantly improving the system's dynamic performance and stability. A FF algorithm based on the Newton-Raphson iteration method is introduced to design the adaptive decoupling networks, which helps to address the nonlinearity of the TAB converter and enhance the system's dynamic performance and controllability. The effectiveness of proposed methods is validated in practical applications with detailed theoretical and experimental studies. The proposed approaches facilitate the broader application of TAB dc/dc converters in the field of charging stations, SST, solar system, and dc microgrid.

## REFERENCES

[1] R. W. A. A. De Doncker, D. M. Divan, and M. H. Kheraluwala, "A three-phase soft-switched high-power-density DC/DC converter for high-power applications," *IEEE Trans. Ind. Appl.*, vol. 27, no. 1, pp. 63–73, Jan./Feb. 1991.

[2] C. Zhao, S. D. Round, and J. W. Kolar, "An isolated three-port bidirectional DC-DC converter with decoupled power flow management," *IEEE Trans. Power Electron.*, vol. 23, no. 5, pp. 2443–2453, Sep. 2008.

[3] H. Tao, A. Kotsopoulos, J. L. Duarte, and M. A. M. Hendrix, "Transformer-coupled multiport ZVS bidirectional DC–DC converter with wide input range," *IEEE Trans. Power Electron.*, vol. 23, no. 2, pp. 771–781, Mar. 2008.

[4] Z. Qi, M. A. Rahman, and M. R. Islam, "Model predictive control for magnetic linked multiport converter," in *Proc. IEEE Glob. Conf. Comput., Power Commun. Technol.*, 2022, pp. 1–6.

[5] Y. Kimura, Y. Yanagi, K. Iwaya, and T. Miyazaki, "A method for decoupling current control of three-port isolated converter," in *Proc. 44th Annu. Conf. IEEE Ind. Electron. Soc.*, 2018, pp. 895–900.

[6] G. Bossi, C. Buccella, C. Cecati, F. Simonetti, and A. Damiano, "A battery-based auxiliary power system for an all-electric aircraft: A novel converter configuration," *IEEE Trans. Ind. Appl.*, vol. 61, no. 6, pp. 9493–9505, Nov./Dec. 2025.

[7] N. Campagna, G. Bossi, R. Miceli, and A. Damiano, "A linearised approach for voltage controller design of inherent decoupled triple active bridge converters," in *Proc. IEEE Energy Convers. Congr. Expo.*, 2024, pp. 2642–2647.

[8] L. Gong et al., "Streamlined QPS control with magnetizing current injection for all-ZVS operation in decoupled-type triple active bridge converters," *IEEE Trans. Power Electron.*, vol. 39, no. 10, pp. 12894–12909, Oct. 2024.

[9] P. Koohi et al., "A dynamically reconfigurable multi-active bridge converter with extended topology-level decoupling," *IEEE Trans. Transp. Electrific.*, vol. 11, no. 5, pp. 11138–11149, Oct. 2025.

[10] P. Zumel, C. Fernandez, A. Lazaro, M. Sanz, and A. Barrado, "Overall analysis of a modular multiactive bridge converter," in *Proc. IEEE 15th Workshop Control Model. Power Electron.*, 2014, pp. 1–9.

[11] J.-Y. Lee and J.-H. Jung, "Modified three-port DAB converter employing voltage balancing capability for bipolar DC distribution system," *IEEE Trans. Ind. Electron.*, vol. 69, no. 7, pp. 6710–6721, Jul. 2022.

[12] F. Wu, K. Wang, and J. Su, "TAB series-resonant DC-DC converter and multi-phase-shift based global optimization modulation," *Appl. Sci.*, vol. 12, 2022, Art. no. 6783.

[13] Y. Wang, F. Han, L. Yang, R. Xu, and R. Liu, "A three-port bidirectional multi-element resonant converter with decoupled power flow management for hybrid energy storage systems," *IEEE Access*, vol. 6, pp. 61331–61341, 2018.

[14] L. Jiang, Y. Wu, L. Gong, Y. Li, J. Xu, and Y. Wang, "Comprehensive online decoupling strategy for LC-TAB converters in EVs considering voltage fluctuation during load transient," *IEEE Trans. Power Electron.*, vol. 39, no. 11, pp. 14518–14532, Nov. 2024.

[15] D. Liu, H. Li, and L. D. Marlino, "Design of A 6 kW multiple-input bi-directional DC-DC converter with decoupled current sharing control for hybrid energy storage elements," in *Proc. IEEE Appl. Power Electron. Conf. Expo.*, 2007, pp. 509–513.

[16] A. Karbozov, M. G. Majumder, H. S. Krishnamoorthy, and K. Rajashekara, "Triple active bridge based multiport energy router for subsea – Renewable interconnection," *IEEE Trans. Ind. Appl.*, vol. 59, no. 4, pp. 4528–4538, Jul./Aug. 2023.

[17] F. Ma, X. Wang, L. Deng, Z. Zhu, Q. Xu, and N. Xie, "Multiport railway power conditioner and its management control strategy with renewable energy access," *IEEE J. Emerg. Sel. Top. Power Electron.*, vol. 8, no. 2, pp. 1405–1418, Jun. 2020.

[18] L. Wang, Z. Wang, and H. Li, "Asymmetrical duty cycle control and decoupled power flow design of a three-port bidirectional DC-DC converter for fuel cell vehicle application," *IEEE Trans. Power Electron.*, vol. 27, no. 2, pp. 891–904, Feb. 2012.

[19] G. Buticchi, L. F. Costa, D. Barater, M. Liserre, and E. D. Amarillo, "A quadruple active bridge converter for the storage integration on the more electric aircraft," *IEEE Trans. Power Electron.*, vol. 33, no. 9, pp. 8174–8186, Sep. 2018.

[20] S. Falcones, R. Ayyanar, and X. Mao, "A DC–DC multiport-converter-based solid-state transformer integrating distributed generation and storage," *IEEE Trans. Power Electron.*, vol. 28, no. 5, pp. 2192–2203, May 2013.

[21] M. Phattanasak, R. Gavagsaz-Ghoachani, J.-P. Martin, B. Nahid-Mobarakeh, S. Pierfederici, and B. Davat, "Control of a hybrid energy source comprising a fuel cell and two storage devices using isolated three-port bidirectional DC–DC converters," *IEEE Trans. Ind. Appl.*, vol. 51, no. 1, pp. 491–497, Jan./Feb. 2015.

[22] P. Koohi, A.J. Watson, J.C. Clare, T.B. Soeiro, and P.W. Wheeler, "A survey on multi-active bridge DC-DC converters: Power flow decoupling techniques, applications, and challenges," *Energies*, vol. 16, 2023, Art. no. 5927.

[23] Y. Chen, P. Wang, H. Li, and M. Chen, "Power flow control in multi-active-bridge converters: Theories and applications," in *Proc. IEEE Appl. Power Electron. Conf. Expo.*, 2019, pp. 1500–1507.

[24] Y. Chen, P. Wang, Y. Elasser, and M. Chen, "Multicell reconfigurable multi-input multi-output energy router architecture," *IEEE Trans. Power Electron.*, vol. 35, no. 12, pp. 13210–13224, Dec. 2020.

[25] Y. Cai, C. Gu, J. Li, J. Yang, G. Buticchi, and H. Zhang, "Dynamic performance enhancement of a triple active bridge with power decoupling-based configurable model predictive control," *IEEE Trans. Transp. Electrific.*, vol. 9, no. 2, pp. 3338–3349, Jun. 2023.

[26] A. H. A. Adam et al., "Power decoupling enhancement of a triple active bridge converter with feedforward compensation based on model predictive control and fuzzy logic controller in DC microgrid systems," *IEEE Access*, vol. 12, pp. 140310–140328, 2024.

[27] G. Buticchi, A. Farjudian, J. Oh, and L. Tarisciotti, "An ANN-assisted control for the power decoupling of a multiple active bridge DC-DC converter," in *Proc. 48th Annu. Conf. IEEE Ind. Electron. Soc.*, 2022, pp. 1–6.

[28] M. Liao, H. Li, P. Wang, T. Sen, Y. Chen, and M. Chen, "Machine learning methods for feedforward power flow control of multi-active-bridge converters," *IEEE Trans. Power Electron.*, vol. 38, no. 2, pp. 1692–1707, Feb. 2023.

[29] H. Ren, Y. Wang, H. Yu, B. Zhang, and Z. Chen, "Deep reinforcement learning-based power flow control for triple active bridge converter," in *Proc. IEEE 10th Int. Power Electron. Motion Control Conf.*, 2024, pp. 2107–2112.

[30] K. Wu, Y. Ma, X. Xiao, and H. Wang, "A hybrid power decoupling strategy for triple active bridge," in *Proc. IEEE 10th Int. Power Electron. Motion Control Conf.*, 2024, pp. 1752–1757.

[31] S. Gong et al., "Sliding mode control-based decoupling scheme for quad-active bridge DC–DC converter," *IEEE J. Emerg. Sel. Top. Power Electron.*, vol. 10, no. 1, pp. 1153–1164, Feb. 2022.

[32] S. Bandyopadhyay, Z. Qin, and P. Bauer, "Decoupling control of multi-active bridge converters using linear active disturbance rejection," *IEEE Trans. Ind. Electron.*, vol. 68, no. 11, pp. 10688–10698, Nov. 2021.

[33] J. Han, X. Li, Y. Sun, S. Gong, and S. Huang, "Optimal design and decoupling control of series DC-link voltages for quadruple active-bridge based UPQC," *Int. J. Elect. Power Energy Syst.*, vol. 140, 2022, Art. no. 108038.

[34] Z. Laiyong, T. Chunming, X. Fan, and L. Peiqiang, "Current stress optimization control of maximum power port of triple active bridge converter based on power becoupling modulation," in *Proc. 5th Int. Conf. Power Eng.*, 2024, pp. 74–83.

[35] C. Gammeter, F. Krismer, and J. W. Kolar, "Comprehensive conceptualization, design, and experimental verification of a weight-optimized all-SiC 2 kV/700 V DAB for an airborne wind turbine," *IEEE J. Emerg. Sel. Top. Power Electron.*, vol. 4, no. 2, pp. 638–656, Jun. 2016.

[36] W. L. Luyben, "Distillation decoupling," *AIChE*, vol. 16, no. 2, pp. 198–203, Mar. 1970.

[37] H. L. Wade, "Inverted decoupling: A neglected technique," *ISA Trans.*, vol. 36, pp. 3–10, 1997.

**Hui Cao** (Student Member, IEEE) received the B.S. degree in electrical engineering from Shandong University, Jinan, China, in 2014, and the M.S. degree in electrical engineering from RWTH Aachen University, Aachen, Germany, in 2020. He is currently working toward the Ph.D. degree in power electronics with the University of Arkansas, Fayetteville, AR, USA.

His research interests include dc/dc converters (DAB/TAB and resonant converters), multilevel inverters, and SiC device.

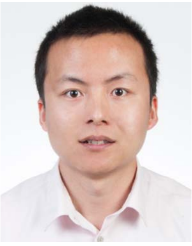

**Guangqi Zhu** (Member, IEEE) received the B.S. and M.S. degrees in electromechanical engineering from the Harbin Institute of Technology, Harbin, China, in 2011 and 2013, respectively, and the Ph.D. degree in electromechanical engineering from the University of Wisconsin at Madison, Madison, WI, USA, in 2018.

He worked as a Senior Specialist Engineer of power conversion with Eaton Research Labs, Menomonee Falls, WI, USA. His research interests include wireless power transfer, high-frequency magnetics design, and high-frequency resonant converter design.

**Xinze Li** (Member, IEEE) received the bachelor's degree in electrical engineering from Shandong University, Shandong, China, in 2018, and the Ph.D. degree in electrical and electronic engineering from Nanyang Technological University, Singapore, in 2023.

In 2024, he joined the University of Arkansas, Fayetteville, AR, USA, as a Research Fellow and Lecturer. His research interests include power converter design, design process automation, light and explainable AI for power electronics with physics-informed systems, and the application of AI in power electronics.

**Peyman Darvish** (Graduate Student Member, IEEE) received the B.Eng. degree in electrical engineering from University Tenaga Nasional, Kajang, Malaysia, in 2017, and the M.Sc. degree in electrical engineering from the University of Malaya (UM), Kuala Lumpur, Malaysia, in 2021. He is currently working toward the Ph.D. degree in electrical engineering with the University of Arkansas, Fayetteville, AR, USA.

He served as a Team Leader with the University of Malaya, in 2022, and was involved in several projects with the Power Electronics and Renewable Energy Research Laboratory (PEARL) in Kuala Lumpur until 2023. His research interests include dc/dc converter and wireless power transfer technologies.

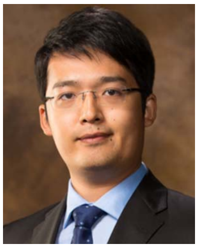

**Yue Zhao** (Senior Member, IEEE) received the B.S. degree in electrical engineering from Beijing University of Aeronautics and Astronautics, Beijing, China, in 2010, and the Ph.D. degree in electrical engineering from the University of Nebraska-Lincoln, Lincoln, USA, in 2014.

He was an Assistant Professor with the Department of Electrical and Computer Engineering, the Virginia Commonwealth University, Richmond, USA, in 2014–2015. Since August 2015, he has been with the University of Arkansas (UA), Fayetteville, USA, where he is currently an Associate Professor with the Department of Electrical Engineering. He also serves as the Executive Director for the National Science Foundation (NSF) I/UCRC on GRid-connected Advanced Power Electronic Systems (GRAPES). He has four U.S. patents granted and coauthored more than 150 papers in refereed journals and international conference proceedings. His current research interests include electric machines and drives, power electronics, and renewable energy systems.

Dr. Zhao is an Associated Editor for IEEE JOURNAL OF EMERGING AND SELECTED TOPICS IN POWER ELECTRONICS (JESTPE) and IEEE OPEN JOURNAL OF POWER ELECTRONICS. He was a recipient of the 2025 John L. Imhoff Outstanding Research Award, the 2020 IEEE Industry Applications Society Andrew W. Smith Outstanding Young Member Achievement Award, and the 2018 NSF CAREER Award.